PHOTONICS Research

Ultrafast miniaturized GaN-based optoelectronic proximity sensor

Xiaoshuai An,[1,2] Hongying Yang,[1] Yumeng Luo,[1] Zhiqin Chu,[2,3,6] and Kwai Hei Li[1,4,5,7]

[1]School of Microelectronics, Southern University of Science and Technology, Shenzhen 518055, China
[2]Department of Electrical and Electronic Engineering, The University of Hong Kong, Hong Kong, China
[3]School of Biomedical Sciences, The University of Hong Kong, Hong Kong, China
[4]Engineering Research Center of Integrated Circuits for Next-Generation Communications, Ministry of Education, Southern University of Science and Technology, Shenzhen 518055, China
[5]Engineering Research Center of Three Dimensional Integration in Guangdong Province, Southern University of Science and Technology, Shenzhen 518055, China
[6]e-mail: zqchu@eee.hku.hk
[7]e-mail: khli@sustech.edu.cn

Received 5 May 2022; revised 20 June 2022; accepted 28 June 2022; posted 28 June 2022 (Doc. ID 462933); published 28 July 2022

In this work, a novel ultrafast optoelectronic proximity sensor based on a submillimeter-sized GaN monolithic chip is presented. Fabricated through wafer-scale microfabrication processes, the on-chip units adopting identical InGaN/GaN diode structures can function as emitters and receivers. The optoelectronic properties of the on-chip units are thoroughly investigated, and the ability of the receivers to respond to changes in light intensity from the emitter is verified, revealing that the sensor is suitable for operation in reflection mode. Through a series of dynamic measurements, the sensor is highly sensitive to object movement at subcentimeter distances with high repeatability. The sensor exhibits ultrafast microsecond response, and its real-time monitoring capability is also demonstrated by applying it to detect slight motions of moving objects at different frequencies, including the human heart rate, the vibration of the rotary pump, the oscillation of the speaker diaphragm, and the speed of the rotating disk. The compact and elegant integration scheme presented herein opens a new avenue for realizing a chip-scale proximity sensing device, making it a promising candidate for widespread practical applications.

https://doi.org/10.1364/PRJ.462933

1. INTRODUCTION

Proximity sensors capable of converting information on the movement of nearby objects into electrical signals without physical contact are of great significance in a wide range of applications, such as mobile robotics, human–machine interactions, inspection in industrial manufacturing processes, production lines, and conveyors [1–4]. Various types of methods have been reported to achieve effective proximity sensing, the most common of which are based on the magnetic, capacitive, and inductive [5–9]. Alternatively, proximity detections via optical techniques have high potential due to their advantages of fast response, high sensitivity, and immunity to electromagnetic interference [10–12]. Operating in reflection/transmission modes, the optoelectronic sensors are typically implemented by assembling two basic components of an illumination source and a photodetector. The presence or absence of an object near the sensing elements varies the reflected/transmitted light, and the detected signals can be analyzed to determine its proximity status.

To meet the ongoing demand for highly portable miniaturized systems, the development of rapid, compact, robust, and lightweight proximity sensors has become more urgent. Recently, proximity measurement based on organic light-emitting diodes (OLEDs) and photodiodes (OPDs) has been reported [13–15], revealing the potential for large-scale on-chip integration. Alternatively, inorganic GaN-based semiconductors and its alloys are the ideal material for developing light-emitting devices, which provide distinct performance over their organic counterparts in terms of efficiency, lifespan, response time, and physical and chemical stability [16–18]. Moreover, monolithic integration of multiple GaN-based optical and electrical components has been demonstrated to be an effective means to enhance the ease of fabrication, compactness, robustness, and functionality [19–22]. In particular, on-chip integration of high-performance GaN-based components, including light-emitting diodes (LEDs), high-electron mobility transistors (HEMTs), waveguides, and photodiodes (PDs), has been reported to form microoptoelectronic systems [23–25].

Although recent experimental studies on optical detection have been proposed together with the demonstrations of potential applications, such as stabilizing the intensity output of LED light sources [26] and detecting the heart pulse in contact mode [27], proximity sensors based on GaN material platforms remain unexploited. In this work, the fabrication of an ultra-compact chip-scale sensor is demonstrated for proximity measurement. The InGaN–diode structures can function as emitters and receivers, fabricated on a GaN-on-sapphire wafer in a flip-chip configuration by a monolithic integration approach. The proposed sensor with multiple sensing units can operate in a noncontact mode, potentially enhancing its measurement flexibility in various practical applications. Apart from the optoelectronic characteristic of the on-chip components, extensive measurements are carried out to validate the proposed proximity instrument and demonstrate its real-time monitoring capability under different dynamic conditions.

2. EXPERIMENTAL SECTION

On-chip sensing units with the same diode-based structure are simultaneously fabricated on a GaN-on-sapphire wafer using standard microfabrication techniques, as schematically depicted in Fig. 1(a). Grown by metal-organic chemical vapor deposition (MOCVD) on a 4-in. sapphire substrate, the epitaxial structure consists of 3-μm undoped GaN (μ-GaN), 2.5-μm Si-doped GaN (n-GaN), 14-pair $In_{0.16}Ga_{0.84}N$ (2.5 nm)/GaN (10 nm) multiquantum wells (MQWs), and 0.2 μm of Mg-doped (p-GaN). Processing of the wafers begins with the deposition of a 200-nm thick indium–tin–oxide (ITO) current spreading layer over p-GaN as a p-contact layer. The 310 μm × 310 μm mesa regions are formed by photolithography, and the unmasked GaN regions are etched to expose the n-GaN surface by inductively coupled plasma (ICP) etching. A Cr/Al/Ti/Pt/Au/Ti layer as electrodes is deposited by electron-beam evaporation. The remaining GaN regions between the units are fully removed via photolithography combined with ICP etching. A SiO_2 passivation layer with a thickness of 0.36 μm is coated by plasma-enhanced chemical vapor deposition. A 3.16-μm-thick distributed Bragg reflector (DBR), which consists of 23 pairs of alternately stacked TiO_2 and SiO_2 layers, is deposited by an optical thin-film coater (Optorun OTFC-1300DBI). During the coating process, the reflectance of the sample is monitored, and the layer thickness is modified according to the referenced reflectance signals, resulting in the thickness variation of TiO_2 and SiO_2 layers in the range of tens to a hundred nanometers. The p-pad and n-pad regions are then defined by photolithography, and metal pads are sequentially electron-beam deposited. The random rough surface of the unpolished sapphire substrate introduces scattering effects on the incoming light, which may lead to unpredictable characteristics of light propagation behavior. To avoid this, the sapphire substrate is polished to a thickness of 200 μm. The diced chip is packaged on an Al-based printed circuit board (PCB) by flip-chip bonding, as shown in Fig. 1(b). The figure inset shows an 880 μm × 880 μm chip, consisting of four identical units, each having a size of 310 μm × 310 μm.

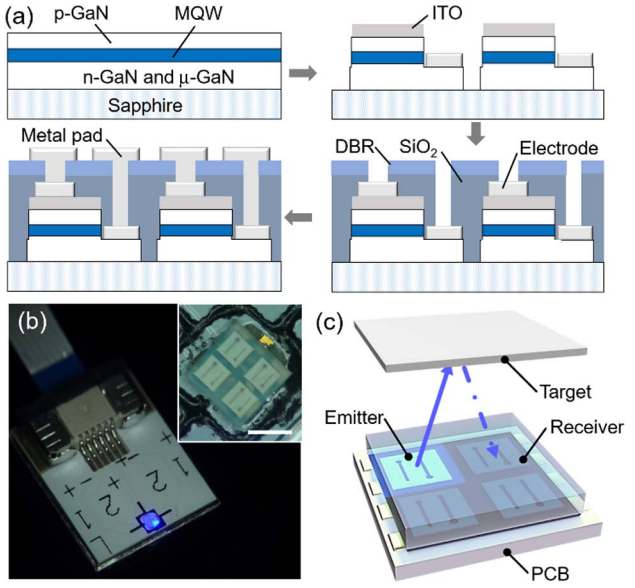

Fig. 1. (a) Schematic diagrams showing the fabrication process flow of the GaN chip. (b) Optical image of the packaged chip; inset shows the enlarged image of the chip. Scale bar is 500 μm. (c) Schematic diagram depicting the operating principle of the proximity sensor.

3. RESULTS AND DISCUSSION

Figure 1(c) depicts the working mechanism of proximity measurement based on the proposed sensor. The on-chip units based on the InGaN diode structure can operate as an emitter and receiver, connected to a current source and ammeter, respectively. In the InGaN layers of the emitter, light emission is generated through the radiative recombination of the confined carriers. The emitted light can be absorbed by the InGaN layers in the receiver to produce an electron–hole pair due to the partial overlap between the emission and the absorption spectra [26,28,29]. The light propagating through the transparent sapphire substrate experiences varying degrees of reflection, depending on the proximity conditions of the object, and the measured photocurrent can be used to reflect its position changes.

The current-voltage (*I-V*) properties of the on-chip units are measured by a Keithley 2450 source meter with a resolution of 50 pA. As an emitter, the forward voltage is measured to be 2.80 V at a driving current of 10 mA, as shown in Fig. 2(a). The dynamic resistance extracted from the slope of the linear region of the *I-V* curve is 15.1 Ω. Figure 2(b) plots the emission spectrum of the emitter with a peak wavelength of 452 nm. As shown in the same figure, the DBR as a bottom reflector provides the reflectance of >0.96 for the spectral range of 410–500 nm. Since the same InGaN/GaN MQWs diode structure is used for light emission and detection, it is important to study the ability of the receiver to detect light from the emitter. Figure 2(c) plots the photocurrent as a function of the voltage of the receiver under different emitter currents. The currents measured under reverse bias voltages are below 1 nA without illumination. The current level increases above 1 μA when the emitter current exceeds 1 mA. The etched sidewalls passivated with the oxide layer can effectively inhibit the

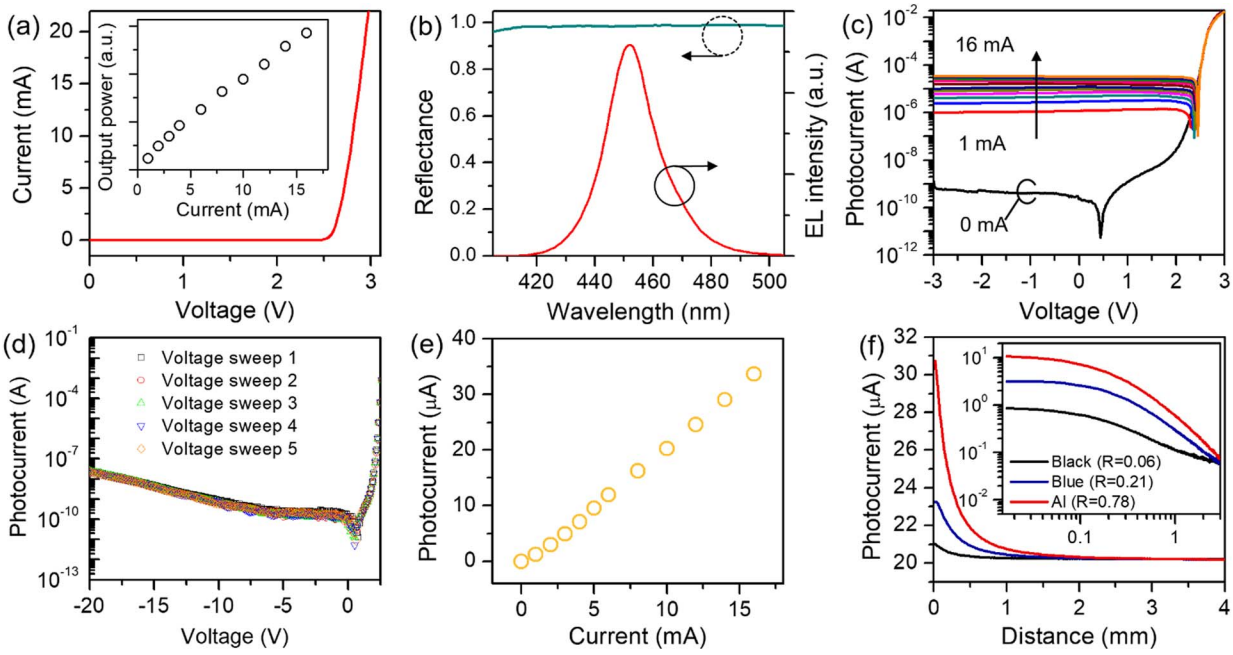

Fig. 2. (a) *I-V* characteristic of the on-chip unit as an emitter. Inset shows the light output intensity as a function of injection current. (b) Emission spectrum of the emitter operating at 10 mA and reflectance plot of the DBR measured at normal incidence; (c) *I-V* characteristic of the on-chip unit as a receiver when the emitter operates at different currents; (d) *I-V* characteristic of the receiver measured at reverse bias voltages of up to −20 V; (e) plot of photocurrent of the receiver versus driving current of the emitter; (f) photocurrent as a function of the distance of the sensor from the films with varying reflectance; inset shows photocurrent change versus the distance of the sensor from the films on a logarithmic scale.

leakage current, resulting in a stable reverse bias current. Moreover, the current at a reverse bias voltage of up to −20 V is less than 10^{-7} A, and the receiver can function properly without damage after multiple voltage sweeps, as illustrated in Fig. 2(d). Extracted from Fig. 2(c), the photocurrent of the unbiased receiver as a function of the current of the emitter is plotted in Fig. 2(e). The highly linear behavior implies that the detected photocurrent can be used to indicate the changes in reflected light intensity. When the driving current of the emitter increases from 1 to 16 mA, the change in photocurrent rises monotonically from 1.2 to 33.7 μA.

To investigate the ability of the sensor to detect objects, Al foil, blue- and black-colored films with different reflectance ($R = 0.78$, 0.21, and 0.06 at normal incidence) to blue emission are placed at different intervals from the sensor. During the measurement, the emitter is biased at 10 mA, and the movements of Al foil and colored films are controlled by a motorized stage. From the curves plotted in Fig. 2(f), it can be seen that the change in measured photocurrent decreases with the increase of the distance from the sensor for both Al foil and colored films. Although the reflectance of the Al foil is known to decrease with increasing incidence angle [30], the Al foil can still introduce more significant changes in photocurrent compared with the colored films. The photocurrents are plotted on a logarithmic scale in the inset of Fig. 2(f), indicating that the sensor can respond to a distance of up to 3 mm from the sensor.

The transient response of the sensor is investigated by biasing the emitter with a 50% duty-cycle square wave at 50 kHz supplied by a signal generator (RIGOL DG1022Z), and the photovoltage signals are measured using a Stanford Research Systems SR570 current preamplifier connected to a Tektronix MDO32 3-BW-100 oscilloscope. Figure 3(a) shows the results measured when the square wave signals with different high levels and with the same low level of 0 V are injected into the emitter. For the applied voltage level of 2.8 V, the rise and fall times, defined as the time required for signals to reach the steady maximum/minimum values, are found to be 3.5 and 3.6 μs, which are the fastest response time of proximity sensors ever reported in the literature [31–35]. With the increasing high voltage levels to 3.0 and 3.2 V, the rise and fall times are found to be nearly identical, as shown in Fig. 3(a). The fast response time of the proximity sensor can be attributed to the rapid photoelectric conversion in the emitter and detector employing the InGaN/GaN diode structure. The fast radiative recombination rate in the InGaN/GaN MQWs enables high-speed emitters, and the miniature device can effectively reduce the resistive-capacitive (RC) decay for the photoelectric conversion [36]. Different from hybrid assembly methods used in the reported proximity sensing units shown in Table 1, the monolithic integration design together with wafer-scale fabrication techniques can not only reduce the size of InGaN/GaN diode units to the submillimeter scale, but also make low-cost, large-scale and high-density integration possible. The total cost of each fabricated chip, along with the PCB package, is less than 0.50 USD. It is also worth noting that the size and response/recovery times of the proposed sensor remain superior compared to the commercial ones listed in Table 1.

To evaluate the dynamic characteristics of the sensor, a circular Al foil with a diameter of 6 mm is attached to the end of an optical post and a motorized stage (Zolix PSA200-11-X)

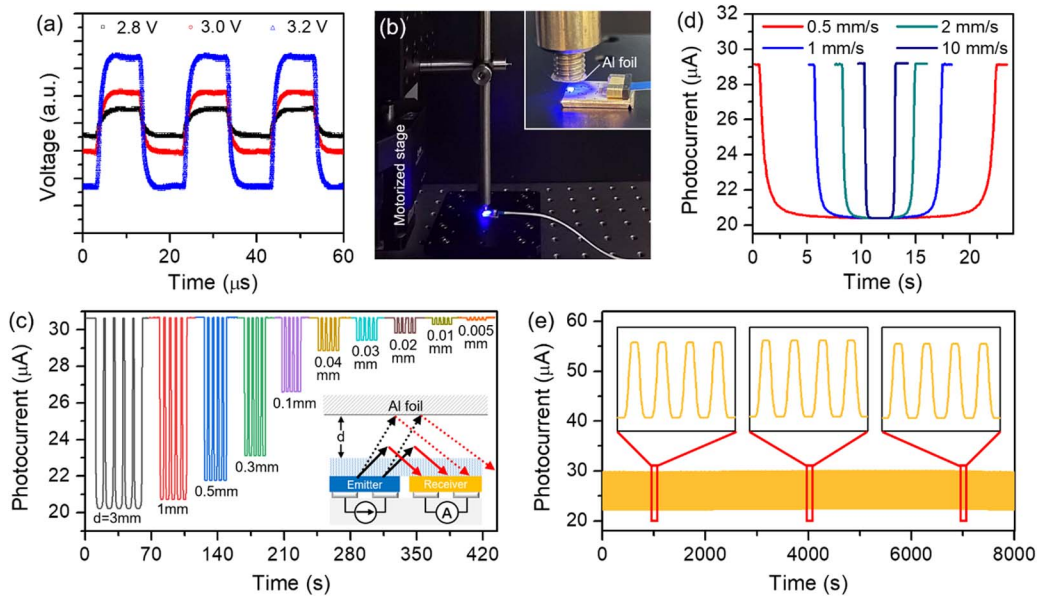

Fig. 3. (a) Transient response of the sensor. The emitter is biased with square waves with high voltage levels of 2.8 V, 3.0 V, and 3.2 V. (b) Optical image of the experimental setup used to measure the dynamic response of the sensor. The inset shows a close-up image. (c) Dynamic response measured from an Al foil moving back and forth repeatedly at different distances from the surface of the sensor. Inset shows the schematic of experimental measurement. (d) Measured photocurrent under one cyclic movement of Al foil between $d = 0.035$ mm and $d = 3$ mm at different speeds; (e) measured photocurrent distribution of the sensor over 8000 cycles under the conditions of back-and-forth motion between $d = 0.015$ mm and $d = 0.4$ mm and a speed of 1 m/s. The emitter current is fixed at 10 mA for the measurement for (c)–(e).

Table 1. Comparison with Other Reported Work and Commercial Products

Structure	Mechanism	Number of Units	Size	Res./Rec. Time[a]	Price (USD)
Graphene nanoplatelets, carbon black and silicone rubber [1]	Capacitive and resistive	1	8 mm × 12 mm	0.27 s	/
Metal electrodes and graphene nanoplatelets [5]	Capacitive and resistive	8 × 8	Each unit: 5 mm × 10 mm	0.24 s	/
Organic thin film [35]	Semiconductor	6 × 6	>4 cm	480 ms	/
Commercial reflective photosensors [34]	Optoelectronic	5 × 5	Each unit: 4.9 mm × 6.4 mm × 6.5 mm	1 ms	/
Organic photodetector on LED [11]	Optoelectronic	1	Active region: 3.57 mm^2	40 cs/20 cs	/
Electrostatic gating [33]	Electrostatic	1	Not shown	5.42 s/11.65 s	/
LEDs and photodiode [12]	Optoelectronic	8	20 mm × 30 mm × 40 mm	<1 ms	/
CA30CAN25NA	Capacitive	1	30 mm × 81 mm (Φ × L)	<10 ms	~10
Panasonic-EQ-501	Optoelectronic	1	68 mm × 68 mm × 26 mm	<20 ms	~70
ORMON-E2J-W10MA	Capacitive	1	20 mm × 5.5 mm × 30 mm	70 Hz/min	~40
SUNX-EX-28 A	Optoelectronic	1	8.2 mm × 10.5 mm × 22 mm	<0.5 ms	~30
GaN optoelectronic devices	**Optoelectronic**	**2 × 2**	**0.88 mm × 0.88 mm × 0.21 mm**	**3.5 μs/3.6 μs**	<0.5

[a]Response/recovery times.

equipped with a motion controller (Zolix MC600-4B) is used to control the movement of the Al foil, as shown in Fig. 3(b). The instantaneous photocurrent response of the sensor is obtained by moving an Al foil back and forth repeatedly at distances d from the sensors, as illustrated in the inset in Fig. 3(c). For d in two different ranges of 0.005–0.04 mm and 0.1–3 mm, the speed is set to 0.05 mm/s and 1 mm/s, respectively. As shown in Fig. 3(c), in the five repetitive cycles of each routine, the photocurrents can consistently reach the lowest levels and return to the same initial value, revealing the high repeatability of the sensor. Moreover, symmetric profiles of measured photocurrents are obtained when detecting an object moving back and forth at different speeds from 0.5 to 10 mm/s, as shown in Fig. 3(d). This also implies that the speed does not affect the initial value, and the measured readings can return to their initial values. The long-term durability and stability are examined by cyclic tests. Repeated back and forth movements between $d = 0.015$ mm and $d = 0.4$ mm and a speed of 1 mm/s are applied to the Al foil. There is a holding time of 1 s when the Al foil reaches its initial and final positions. As shown in Fig. 3(e), the readout signals are highly stable throughout 8000 cycles, and the photocurrent profiles of the three different periods in the figure inset are almost identical, which confirms the durability and stability of the sensor.

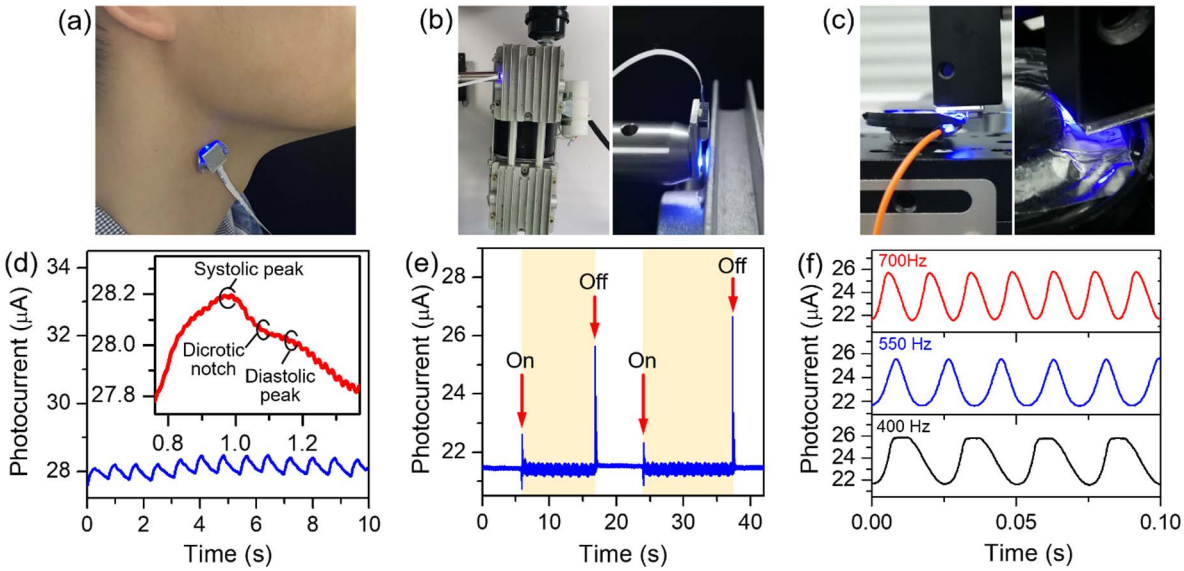

Fig. 4. Sensor for real-time monitoring. Optical images of the sensor mounted on (a) volunteer's neck, and close to (b) mechanical pump, (c) speaker diaphragm; (d)–(f) photocurrent profiles measured from the corresponding conditions in (a)–(c); the driving current of the emitter is fixed at 10 mA.

Having identified that the proposed proximity sensor is highly sensitive to slight distance changes of objects with fast response, the real-time monitoring capability of the chip-scale device in practical applications is studied. Prior to measurement, the target object is affixed with a small piece of Al foil to increase the amount of reflected light. First, the sensor is mounted on a volunteer's neck and a clear oscillating heart rate signal with a frequency of about 1.3 Hz is obtained, as shown in Figs. 4(a) and 4(d). By enlarging the waveform shown in the inset of Fig. 4(d), detailed information about the blood pressure profile, including a diastolic notch, systolic peak, and diastolic peak can be identified. Then, the sensor is fixed adjacent to the rotary pump, as displayed in Fig. 4(b). It is known that the frequency and amplitude of vibration signal are the key parameters to indicate the operation condition and fault diagnosis of the rotary pump [37], and such noncontact measurement is a direct and simple means. From the results shown in Fig. 4(e), the observation of the sudden increases in photocurrents represents a large extent of vibration at the instant of switching the pump on and off. Between the two distinct on and off signals, a constant frequency of ~30 Hz corresponding to the working frequency of the pump is obtained.

To further testify the ability to detect higher-frequency oscillations, the sensor is mounted close to a commercial speaker with a diameter of 2.9 cm and a working frequency of several hundred hertz, as shown in Fig. 4(c). As illustrated in the plot in Fig. 4(f), the speaker diaphragm vibrating at frequencies of 400, 550, and 700 Hz can be observed. Apart from recognizing the object movement in the vertical direction, detections along the lateral direction are investigated. The sensor is placed close to a white- and black-painted disk equipped on a motorized spinner, as shown in Fig. 5(a). The photocurrent difference of >1 μA is observed for the disk rotating at thousands of rotations per minute (r/min), and stepwise responses are displayed at high speeds up to 8000 r/min, as evident in Fig. 5(b).

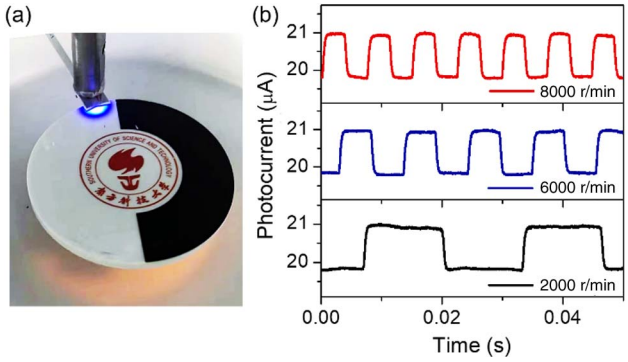

Fig. 5. (a) Optical image of the sensor mounted close to rotating disk half-painted in black and white; (b) photocurrent profiles measured from the disk at different rotating speeds when the emitter current is 10 mA.

When an on-chip unit acts as an emitter, the others can act as receivers in response to objects in their vicinity. To study this, Al foils of different shapes are placed on the detecting units using the micropositioners (SIGNATONE S-725). As shown in Fig. 6, a sharp contrast of photocurrent levels between the covered and uncovered units can be obtained. For the coverage of a single unit, the photocurrent changes show more than 0.15 μA, which is more than 3 times larger than that of the uncovered ones, as shown in Figs. 6(b)–6(d). Notably, increasing the number of covered units can promote the amount of reflected light, resulting in readout levels exceeding 0.20 and 0.25 μA for double- and triple-covered units, respectively, as shown in Figs. 6(e)–6(g). With the obvious contrast between the measured photocurrents, the sensor can be used to detect small objects overlaid on the units.

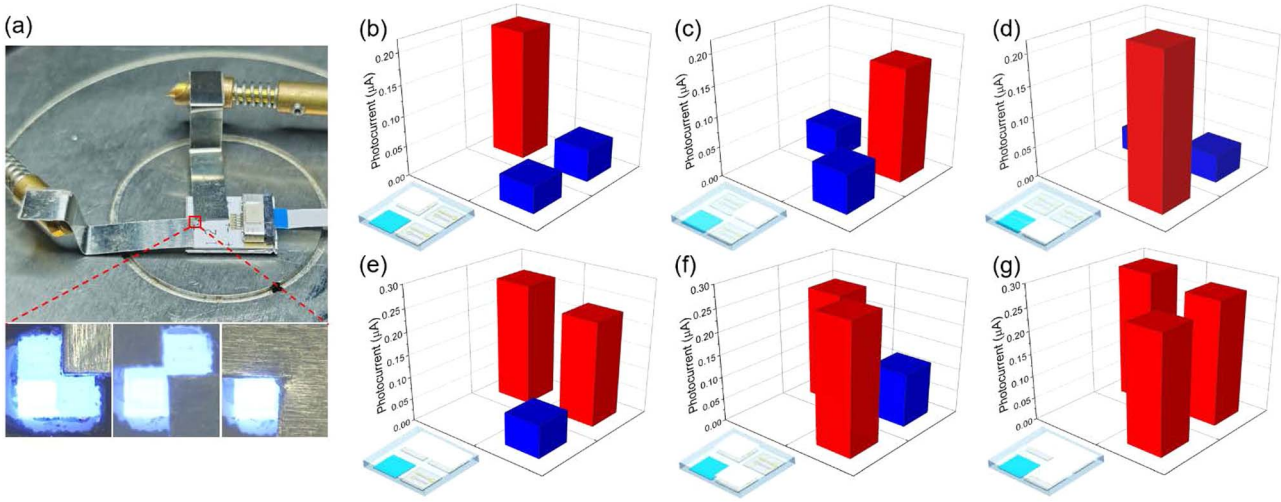

Fig. 6. (a) Optical images showing the selective area coverage of the Al foils on the sensor using the micropositioners; distributions of photocurrent changes of units acting as receivers when Al foil is overlaid on (b)–(d) single, (e), (f) double, and (g) triple units. The emitter operates at a low current of 1 mA.

4. CONCLUSION

In summary, an ultracompact sensor based on the same InGaN/GaN MQW diode structure as the emitters and receiver is demonstrated for proximity measurement. The electrical and optical properties of the on-chip units are investigated, demonstrating the ability to detect objects in the subcentimeter range. The sensor with microsecond response times can respond to the object movements in different dynamic conditions. Fabricated through extendable wafer-scale processes, the proposed proximity sensor provides submillimeter size, fast response, ease of operation, and high repeatability, which makes it well suited for practical applications requiring real-time monitoring.

Funding. NSQKJJ (K20799112); HKSAR Research Grants Council (RGC) Early Career Scheme (27202919); Shenzhen Natural Science Foundation Stability Support Program Project (20200925160044004); National Natural Science Foundation of China (12074170, 62004088).

Disclosures. The authors declare no conflicts of interest.

Data Availability. Data underlying the results presented in this paper are not publicly available at this time but may be obtained from the authors upon reasonable request.

REFERENCES

1. H. K. Lee, S. I. Chang, and E. Yoon, "Dual-mode capacitive proximity sensor for robot application: implementation of tactile and proximity sensing capability on a single polymer platform using shared electrodes," IEEE Sens. J. **9**, 1748–1755 (2009).
2. A. Braun, R. Wichert, A. Kuijper, and D. W. Fellner, "Capacitive proximity sensing in smart environments," J. Ambient Intell. Smart Environ. **7**, 483–510 (2015).
3. Y. Huang, X. Cai, W. Kan, S. Qiu, X. Guo, C. Liu, and P. Liu, "A flexible dual-mode proximity sensor based on cooperative sensing for robot skin applications," Rev. Sci. Instrum. **88**, 085005 (2017).
4. Y. Ye, C. Y. Zhang, C. L. He, X. Wang, J. J. Huang, and J. H. Deng, "A review on applications of capacitive displacement sensing for capacitive proximity sensor," IEEE Access **8**, 45325–45342 (2020).
5. S. H. Qiu, Y. Huang, X. Y. He, Z. G. Sun, P. Liu, and C. X. Liu, "A dual-mode proximity sensor with integrated capacitive and temperature sensing units," Meas. Sci. Technol. **26**, 105101 (2015).
6. D. J. Sadler and C. H. Ahn, "On-chip eddy current sensor for proximity sensing and crack detection," Sens. Actuators A Phys. **91**, 340–345 (2001).
7. A. Bonen, R. E. Saad, K. C. Smith, and B. Benhabib, "A novel electro-optical proximity sensor for robotics: calibration and active sensing," IEEE Trans. Robot. **13**, 377–386 (1997).
8. X. Lü, X. Li, F. Zhang, S. Wang, D. Xue, L. Qi, H. Wang, X. Li, W. Bao, and R. Chen, "A novel proximity sensor based on parallel plate capacitance," IEEE Sens. J. **18**, 7015–7022 (2017).
9. J. Castellanos-Ramos, A. Trujillo-León, R. Navas-González, F. Barbero-Recio, J. A. Sánchez-Durán, Ó. Oballe-Peinado, and F. Vidal-Verdú, "Adding proximity sensing capability to tactile array based on off-the-shelf FSR and PSOC," IEEE Trans. Instrum. Meas. **69**, 4238–4250 (2019).
10. L. Sant, A. Fant, S. Stojanovic, S. Fabbro, and J. L. Ceballos, "A 13.2 b optical proximity sensor system with 130 klx ambient light rejection capable of heart rate and blood oximetry monitoring," IEEE J. Solid-State Circuits **51**, 1674–1683 (2016).
11. C. H. Chen, C. F. Lin, K. H. Wang, H. C. Liu, H. W. Zan, H. F. Meng, W. Hortschitz, H. Steiner, A. Kainz, and T. Sauter, "High-resolution proximity sensor using flexible semi-transparent organic photo detector," Org. Electron. **49**, 305–312 (2017).
12. K. Koyama, M. Shimojo, T. Senoo, and M. Ishikawa, "High-speed high-precision proximity sensor for detection of tilt, distance, and contact," IEEE Rob. Autom. Lett. **3**, 3224–3231 (2018).
13. L. Bürgi, R. Pfeiffer, M. Mücklich, P. Metzler, M. Kiy, and C. Winnewisser, "Optical proximity and touch sensors based on monolithically integrated polymer photodiodes and polymer LEDs," Org. Electron. **7**, 114–120 (2006).
14. M. Prosa, E. Benvenuti, D. Kallweit, P. Pellacani, M. Toerker, M. Bolognesi, L. Lopez-Sanchez, V. Ragona, F. Marabelli, and S. Toffanin, "Organic light-emitting transistors in a smart-integrated system for plasmonic-based sensing," Adv. Funct. Mater. **31**, 2104927 (2021).
15. H. L. Tam, W. H. Choi, and F. R. Zhu, "Organic optical sensor based on monolithic integration of organic electronic devices," Electronics **4**, 623–632 (2015).

16. A. Laubsch, M. Sabathil, J. Baur, M. Peter, and B. Hahn, "High-power and high-efficiency InGaN-based light emitters," IEEE Trans. Electron Devices **57**, 79–87 (2009).
17. M. Meneghini, L. R. Trevisanello, G. Meneghesso, and E. Zanoni, "A review on the reliability of GaN-based LEDs," IEEE Trans. Device Mater. Reliab. **8**, 323–331 (2008).
18. M. Meneghini, A. Tazzoli, G. Mura, G. Meneghesso, and E. Zanoni, "A review on the physical mechanisms that limit the reliability of GaN-based LEDs," IEEE Trans. Electron Devices **57**, 108–118 (2009).
19. D. Chen, D. Li, G. Zeng, F.-C. Hu, Y.-C. Li, Y.-C. Chen, X.-X. Li, J. Tang, C. Shen, and N. Chi, "GaN-based micro-light-emitting diode driven by a monolithic integrated ultraviolet phototransistor," IEEE Electron Device Lett. **43**, 80–83 (2021).
20. S. Hwangbo, L. Hu, A. T. Hoang, J. Y. Choi, and J.-H. Ahn, "Wafer-scale monolithic integration of full-colour micro-led display using MoS_2 transistor," Nat. Nanotechnol. **17**, 500–506 (2022).
21. Y. Wang, X. Wang, B. Zhu, Z. Shi, J. Yuan, X. Gao, Y. Liu, X. Sun, D. Li, and H. Amano, "Full-duplex light communication with a monolithic multicomponent system," Light Sci. Appl. **7**, 83 (2018).
22. B. Jia, X. Gao, Z. Ye, P. Liu, F. Hu, H. Zhu, and Y. Wang, "Monolithically integrated sensing, communication, and energy harvester," Energy Technol. **10**, 2100793 (2022).
23. Z. Li, J. Waldron, T. Detchprohm, C. Wetzel, R. Karlicek, Jr., and T. Chow, "Monolithic integration of light-emitting diodes and power metal-oxide-semiconductor channel high-electron-mobility transistors for light-emitting power integrated circuits in GaN on sapphire substrate," Appl. Phys. Lett. **102**, 192107 (2013).
24. Y.-J. Lee, Z.-P. Yang, P.-G. Chen, Y.-A. Hsieh, Y.-C. Yao, M.-H. Liao, M.-H. Lee, M.-T. Wang, and J.-M. Hwang, "Monolithic integration of GaN-based light-emitting diodes and metal-oxide-semiconductor field-effect transistors," Opt. Express **22**, A1589–A1595 (2014).
25. C. Liu, Y. Cai, Z. Liu, J. Ma, and K. M. Lau, "Metal-interconnection-free integration of InGaN/GaN light emitting diodes with AlGaN/GaN high electron mobility transistors," Appl. Phys. Lett. **106**, 181110 (2015).
26. K. H. Li, Y. F. Cheung, W. Jin, W. Y. Fu, A. T. L. Lee, S. C. Tan, S. Y. Hui, and H. W. Choi, "InGaN RGB light-emitting diodes with monolithically integrated photodetectors for stabilizing color chromaticity," IEEE Trans. Ind. Electron. **67**, 5154–5160 (2019).
27. L. Chen, Y. Wu, and K. Li, "Monolithic InGaN/GaN photonic chips for heart pulse monitoring," Opt. Lett. **45**, 4992–4995 (2020).
28. R. Martin, P. Middleton, K. O'Donnell, and W. Van der Stricht, "Exciton localization and the Stokes' shift in InGaN epilayers," Appl. Phys. Lett. **74**, 263–265 (1999).
29. J. Yan, L. Wang, B. Jia, Z. Ye, H. Zhu, H. Choi, and Y. Wang, "Uniting GaN electronics and photonics on a single chip," J. Lightwave Technol. **39**, 6269–6275 (2021).
30. M. Janecek and W. W. Moses, "Optical reflectance measurements for commonly used reflectors," IEEE Trans. Nucl. Sci. **55**, 2432–2437 (2008).
31. Y. C. Cai, J. Shen, C. W. Yang, Y. Wan, H. L. Tang, A. A. Aljarb, C. L. Chen, J. H. Fu, X. Wei, K. W. Huang, Y. Han, S. J. Jonas, X. C. Dong, and V. Tung, "Mixed-dimensional MXene-hydrogel heterostructures for electronic skin sensors with ultrabroad working range," Sci. Adv. **6**, eabb5367 (2020).
32. Y. R. Kim, T. L. Phan, K. W. Cho, W. T. Kang, K. Kim, Y. H. Lee, and W. J. Yu, "Infrared proximity sensors based on photo-induced tunneling in van der Waals integration," Adv. Funct. Mater. **31**, 2100966 (2021).
33. V. Kedambaimoole, N. Kumar, V. Shirhatti, S. Nuthalapati, S. Kumar, M. M. Nayak, P. Sen, D. Akinwande, and K. Rajanna, "Reduced graphene oxide tattoo as wearable proximity sensor," Adv. Electron. Mater. **7**, 2001214 (2021).
34. H. Hasegawa, Y. Suzuki, A. G. Ming, K. Koyama, M. Ishikawa, and M. Shimojo, "Net-structure proximity sensor: high-speed and free-form sensor with analog computing circuit," IEEE/ASME Trans. Mechatron. **20**, 3232–3241 (2015).
35. G. S. Lv, H. T. Wang, Y. H. Tong, L. Dong, X. L. Zhao, P. F. Zhao, Q. X. Tang, and Y. C. Liu, "Flexible, conformable organic semiconductor proximity sensor array for electronic skin," Adv. Mater. Interfaces **7**, 2000306 (2020).
36. K. H. Li, W. Y. Fu, Y. F. Cheung, K. K. Y. Wong, Y. Wang, K. M. Lau, and H. W. Choi, "Monolithically integrated InGaN/GaN light-emitting diodes, photodetectors, and waveguides on Si substrate," Optica **5**, 564–569 (2018).
37. E. Egusquiza, C. Valero, D. Valentin, A. Presas, and C. G. Rodriguez, "Condition monitoring of pump-turbines: new challenges," Measurement **67**, 151–163 (2015).